Supplementary information for

Combinatorial Screening of Wide Band-Gap Organic Solar Cell Materials with Open-Circuit Voltage between 1.1 and 1.4 V

Miquel Casademont-Viñas,[a] Daniel Capolat,[a] Arianna Quesada-Ramírez,[a] Matiss Reinfelds,[b] Gregor Trimmel,[b] Matteo Sanviti,[c] Jaime Martín,[cd] Alejandro R. Goñi, [ae] Thomas Kirchartz,[fg] and Mariano Campoy-Quiles*[a]

[a.] *Institut de Ciència de Materials de Barcelona (ICMAB-CSIC), Campus de la UAB, Bellaterra, Barcelona, 08193, Spain. E-mail: mcampoy@icmab.es*
[b.] *Institute for Chemistry and Technology of Materials, NAWI Graz, Graz University of Technology, Stremayrgasse 9, 8010 Graz, Austria*
[c.] *Universidade da Coruña, Campus Industrial de Ferrol, CITENI, 15403 Ferrol, Spain*
[d.] *POLYMAT, 20018 Donostia-SanSebastián, Spain*
[e.] *ICREA, Passeig Lluís Companys 23, E-08010 Barcelona, Spain.*
[f.] *IEK5-Photovoltaik, Forschungszentrum Jülich, Jülich, Germany.*
[g.] *Faculty of Engineering and CENIDE, University of Duisburg-Essen, Duisburg, Germany.*

Section S1: Active layer materials IUPAC names

PTQ10: Poly[(thiophene)-alt-(6,7-difluoro-2-(2- hexyldecyloxy)quinoxaline)]

D18: Poly[(2,6-(4,8-bis(5-(2-ethylhexyl-3-fluoro)thiophen-2-yl)-benzo[1,2-b:4,5-b']dithiophene))-alt-5,5'-(5,8-bis(4-(2-butyloctyl)thiophen-2-yl)dithieno[3',2':3,4;2'',3'':5,6]benzo[1,2-c][1,2,5]thiadiazole)]

PM6: Poly[(2,6-(4,8-bis(5-(2-ethylhexyl-3-fluoro)thiophen-2-yl)-benzo[1,2-b:4,5-b']dithiophene))-alt-(5,5-(1',3'-di-2-thienyl-5',7'-bis(2-ethylhexyl)benzo[1',2'-c:4',5'-c']dithiophene-4,8-dione)]

O-IDFBR: (5Z,5'Z)-5,5'-((7,7'-(6,6,12,12-Tetraoctyl-6,12-dihydroindeno[1,2-b]fluorene-2,8-diyl)bis(benzo[c][1,2,5]thiadiazole-7,4-diyl))bis(methanylylidene))bis(3-ethyl-2-thioxothiazolidin-4-one)

PMI-FF-PMI: 8,8' (6,6,12,12-tetraoctyl-6,12-dihydroindeno[1,2-b]fluorene -2,8-yl)-bis (N-(2,6-diisopropylphenyl)-perylene-3,4-dicarboximide)

IO-4Cl: 3,9-bis[5,6-dichloro-1H-indene-1,3(2H)- dione]-5,5,11,11-tetrakis(4-hexylphenyl)dithieno[2,3-d:2',3'-d']-s- indaceno[1,2-b:5,6-b&'rsquo;]dithiophene

Section S2: Active layer materials Optical characterization

Material	E_{bg}^{k} (eV) (ellipsometry)	LUMO-HOMO (eV)	Difference	Difference (%)
D18	2.064	1.92	-0.144	-6.977
PTQ10	2.010	2.56	0.550	27.363
PM6	1.935	1.94	0.005	0.258
O-IDFBR	2.221	2.05	-0.170	-7.699
PMI-FF-PMI	2.127	2.06	-0.067	-3.150
IO-4Cl	1.888	1.89	0.002	0.106

Table S1: Energy band gap of materials calculation. *Energy band gap of active layer materials calculated as the inflection point of the extinction coefficient (k) measured with ellipsometry (E_{bg}^{k}) compared to the difference between LUMO and HOMO found in literature (shown in Figure 1c). The last two columns correspond to the difference between the two E_{bg} values in absolute value and in percentual value with respect to the ellipsometric value.*

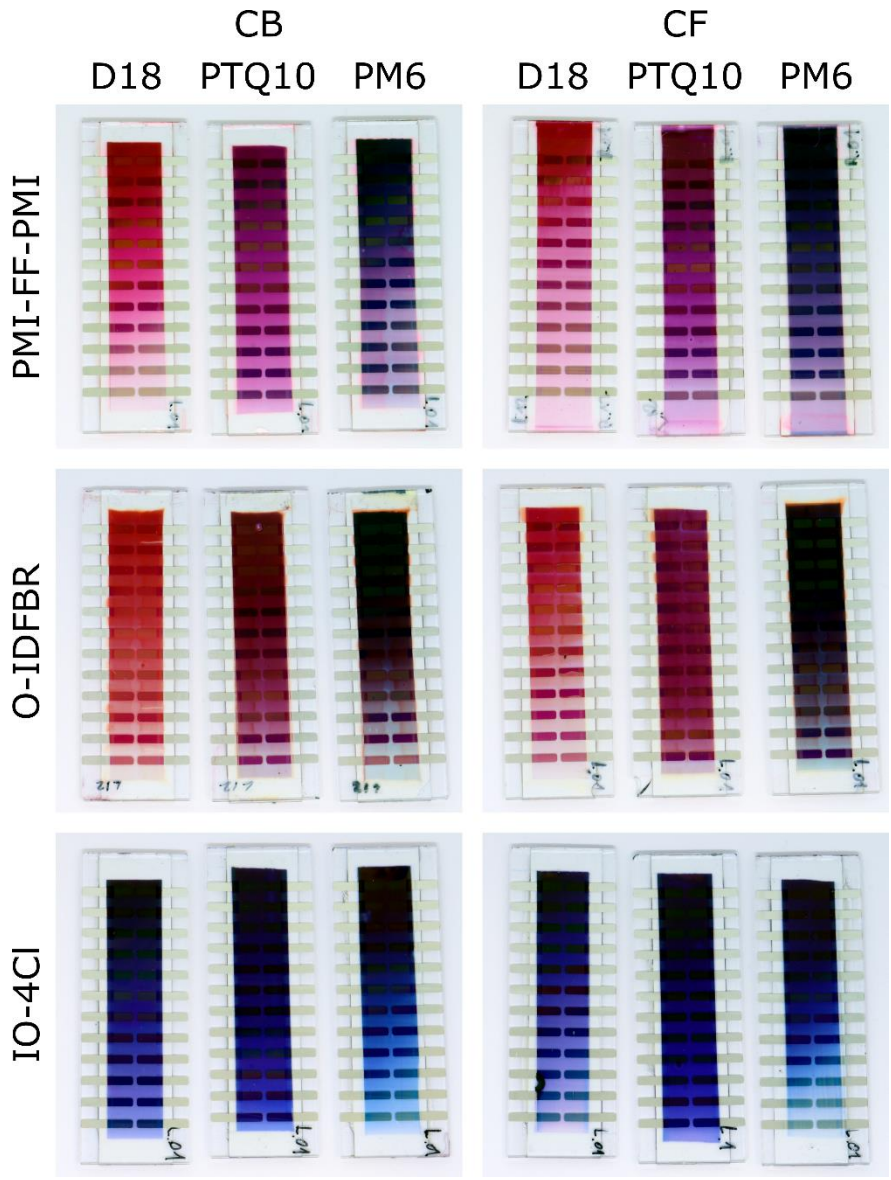

Figure S1: Photographs of all 18 samples prepared in the study. *The color gradient in each sample corresponds to the thickness gradient of the active layer. The different colors of different active layers denote the different band-gaps and absorption profiles of donors and acceptors used. This is also useful to consider for applications where color tunability is useful (semi-transparent OPV, for example).*

Section S3: Benchmarking

Ref.	Active layer			Device geometry	Coating process	V_{oc} [V]	J_{sc} [mA/cm²]	FF [%]	PCE [%]	Area [cm²]
	Donor	Acceptor	Solvent							
[1]	PM6	IO-4Cl	CB	Normal	Spin-coating	1.24	11.6	68.10	9.80	1
[2]	PM6	IO-4Cl	CB	Normal	Spin-coating	1.22	10.42	61.56	7.80	0.04
This work	PM6	IO-4Cl	CB	Inverted	Blade-caoting	1.15	9.00	58.18	6.02	0.08
[3]	D18	PMI-FF-PMI	CB	Normal	Spin-coating	1.41	6.09	60.9	5.34	0.1
This work	D18	PMI-FF-PMI	CB	Inverted	Blade-caoting	1.33	5.35	49.49	3.53	0.08

Table S2: *Comparison between literature work and this work for solar cells made with PM6:IO-4Cl and D18:PMI-FF-PMI deposited from CB as active layer materials.*

Donor	Acceptor	Solvent	V_{oc} [V]	J_{sc} [mA/cm²]	FF [%]	PCE [%]
PTQ10	O-IDFBR	CF	1.33 (1.32)	8.05 (7.39)	50.85 (49.02)	5.44 (4.79)
PTQ10	O-IDFBR*	CB	1.35 (1.35)	9.06 (8.91)	56.05 (54.6)	6.87 (6.57)
PTQ10	PMI-FF-PMI	CF	1.38 (1.36)	3.63 (3.53)	39.52 (38.85)	1.98 (1.87)
PTQ10	PMI-FF-PMI	CB	1.36 (1.35)	1.70 (1.43)	37.80 (36.95)	0.87 (0.82)
PTQ10*	IO-4Cl*	CF	1.25 (1.24)	10.16 (9.79)	57.51 (56.90)	7.31 (6.88)
PTQ10	IO-4Cl	CB	1.22 (1.19)	8.09 (7.78)	56.37 (52.20)	5.55 (4.84)
D18	O-IDFBR	CF	1.29 (1.24)	5.16 (5.17)	47.08 (44.48)	3.15 (2.84)
D18	O-IDFBR	CB	1.33 (1.33)	3.92 (3.81)	50.49 (50.08)	2.62 (2.54)
D18	PMI-FF-PMI	CF	1.28 (1.19)	5.81 (5.42)	42.26 (39.97)	3.14 (2.58)
D18	PMI-FF-PMI*	CB	1.33 (1.31)	5.35 (5.42)	49.49 (46.70)	3.53 (3.31)
D18*	IO-4Cl	CF	1.24 (1.24)	8.32 (7.51)	57.13 (56.88)	5.91 (5.28)
D18	IO-4Cl	CB	1.21 (1.21)	8.13 (7.77)	51.85 (53.29)	5.10 (5.01)
PM6	O-IDFBR	CF	1.23 (1.18)	5.93 (5.50)	41.02 (40.79)	2.99 (2.65)
PM6	O-IDFBR	CB	1.24 (1.22)	4.91 (5.00)	48.95 (47.15)	2.98 (2.87)
PM6	PMI-FF-PMI	CF	1.26 (1.26)	2.20 (2.15)	43.07 (43.19)	1.19 (1.17)
PM6	PMI-FF-PMI	CB	1.26 (1.24)	2.48 (2.47)	52.49 (51.81)	1.64 (1.58)
PM6*	IO-4Cl	CF	1.18 (1.16)	9.29 (9.83)	57.03 (54.30)	6.23 (6.18)
PM6	IO-4Cl	CB	1.15 (1.14)	9.00 (9.33)	58.18 (52.07)	6.02 (5.54)

Table S3: Figures-of-merit from J-V measurements for the best performing devices and their thickness pair. *Although the combinatorial screening high throughput method used lead us explore 18 combinations and 12 thickness for each one, the main problem is that we do not obtain enough data to produce statistical analysis of each cell. This table shows the best performing device for each of the 18 combinations and its thickness pair figure-of-merit is shown in brackets.*

Section S4: V_{oc} dependence on $LUMO_{aceptor}$-$HOMO_{donor}$

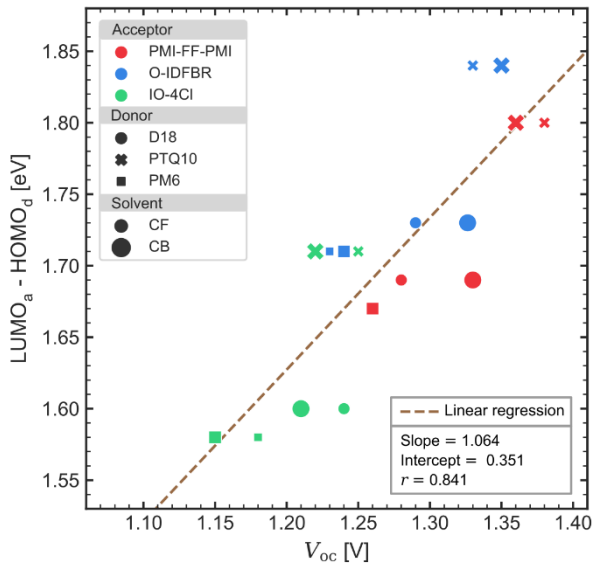

Figure S2: Energy difference between LUMO of the acceptor and the HOMO of the donor as a function of V_{oc}. *The data-points fits to a linear regression with a slope of 1.06 suggesting the direct relation between the $LUMO_{aceptor}$-$HOMO_{donor}$ difference and the V_{oc}. The high Pearsons correlation coefficient (r = 0.84) is also a sign of the strong correlation between the two parameters.*

Section S5: IO-4Cl batches differences

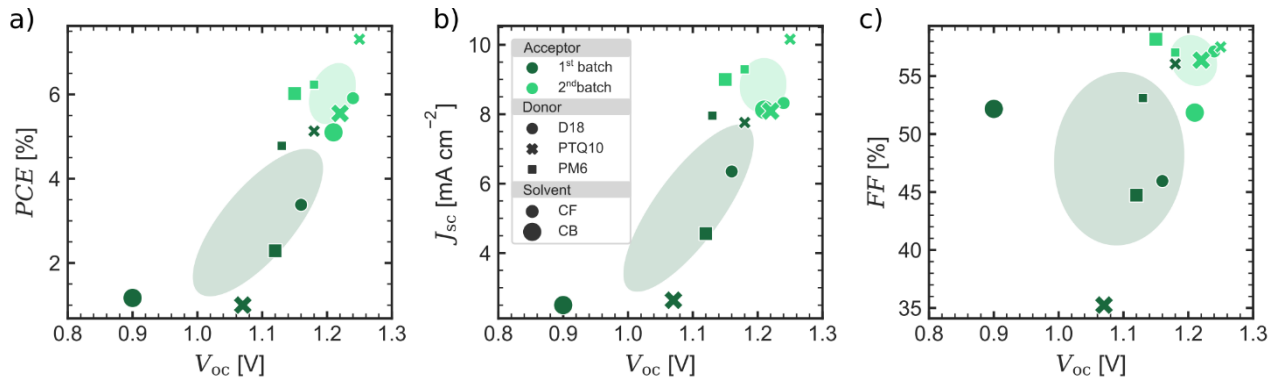

Figure S3: J − V measurements results for the two IO-4Cl batches used. *PCE shows that the second IO-4Cl batch (light green) corresponding to the one discussed in the main manuscript, performs much better than the first used batch (dark green). The first batch lacks mainly from V_{oc} and J_{sc}. These results highlight the importance of differences from batch to batch at the fabrication of materials for the up-scalability of organic solar cells.*

Section S6: GIWAX measurements

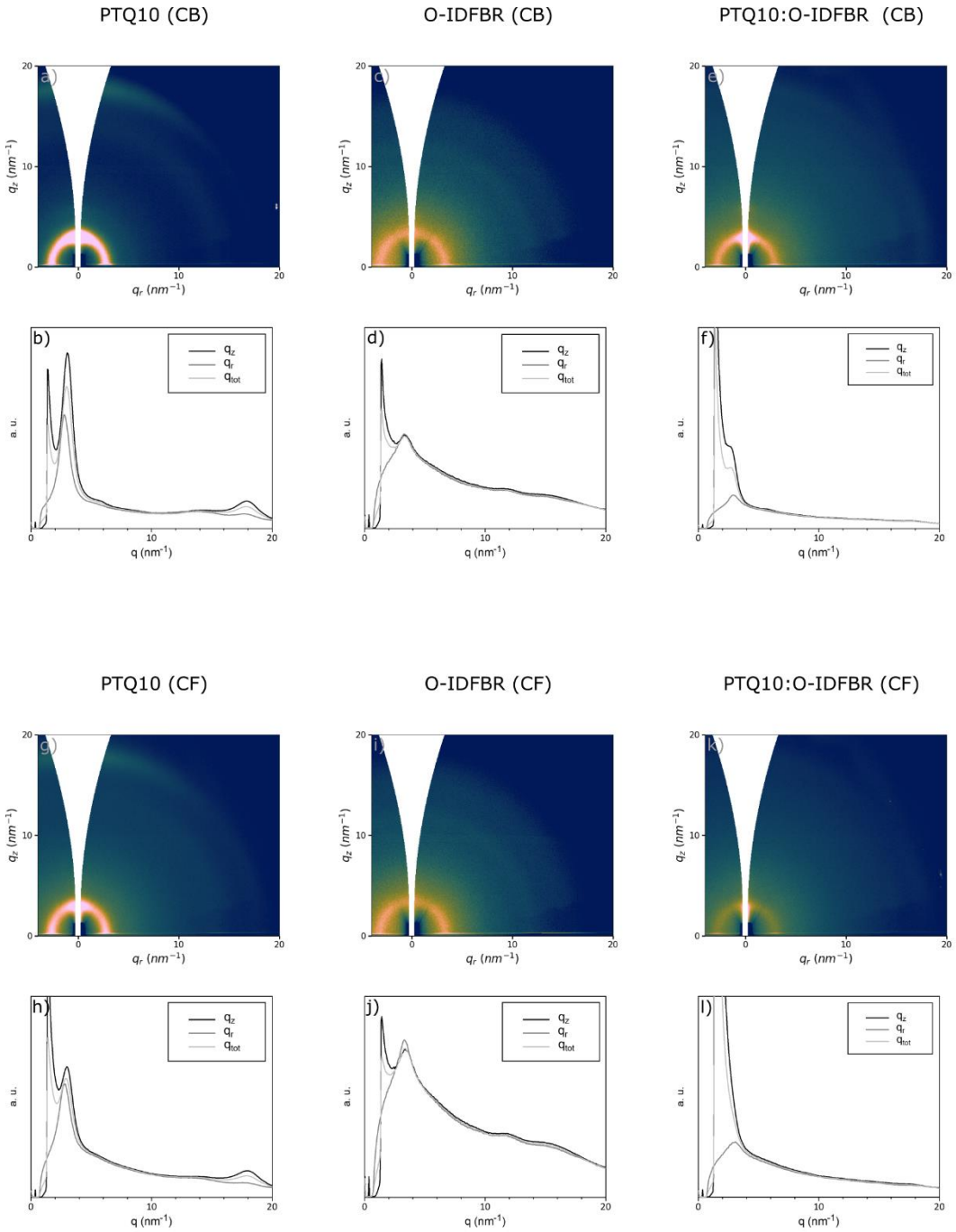

Figure S4: GIWAX data for PTQ10:O-IDFBR deposited from CF and CB.

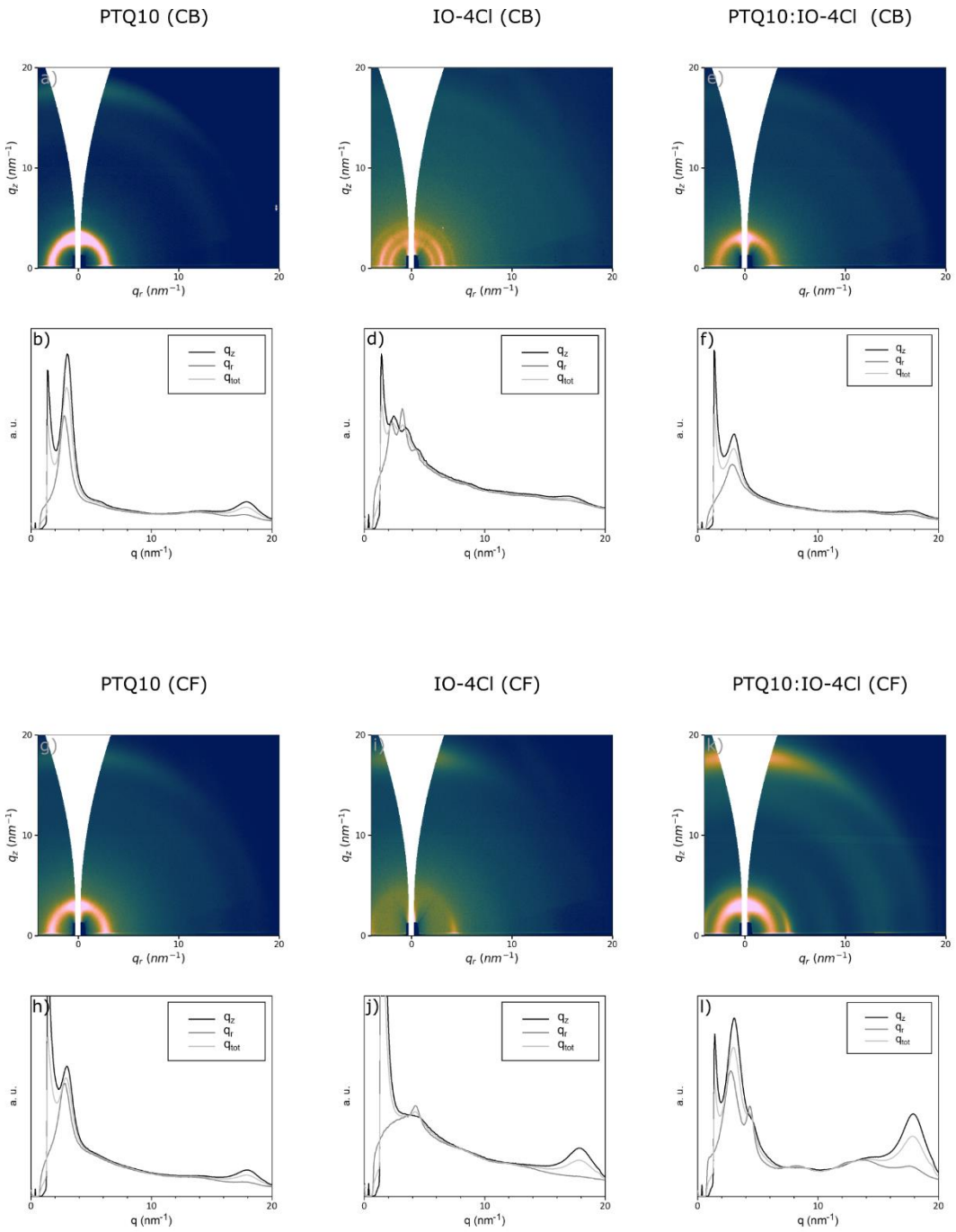

Figure S5: GIWAX data for PTQ10:IO-4Cl deposited from CF and CB.

Sample	Solvent	d [nm]	L_c [nm]	d [nm]	L_c [nm]	d [nm]	L_c [nm]	d [nm]	L_c [nm]	d [nm]	L_c [nm]
		100		010		low q					
PTQ10	CB	2.25	5.79	0.35	2.46						
	CF	2.24	5.48	0.35	2.49						
O-IDFBR	CB					1.90	6.44				
	CF					1.89	6.45				
PTQ10:O-IDFBR	CB	2.13	5.76	0.36	1.99						
	CF	2.09	4.46	-	-						
O-4Cl	CB			0.38	6.13	2.78	20.44	1.99	8.87	1.49	4.88
	CF			0.35	3.25					1.49	10.91
PTQ10:O-4Cl	CB	2.15	5.15	0.36	4.78						
	CF	2.07	5.76	0.35	3.07					1.46	14.82

Table S4: 100 plane, 010 plane and low q region d-spacing (d) and coherence length (L_c) analysis.

The d-spacing (d) and the coherence length (L_c) were collected for all the samples from the 1D integrations of the GIWAXS diffractograms. Data were reported accounting for lamellar stacking of the polymer donor (100 planes) and other contributions, such as π-π stacking (010) as well as characteristic peaks from the acceptors at lower q values.

Compared with the pure donor, the 100 planes of the blends seem to shift towards lower d values. Nevertheless, no direct correlation of such information with structural changes can be directly pointed out, as a contribution from the acceptor at lower q can alter the peak position, making it hard to give reliable assessments.

Section S6: FF vs. V_{oc}

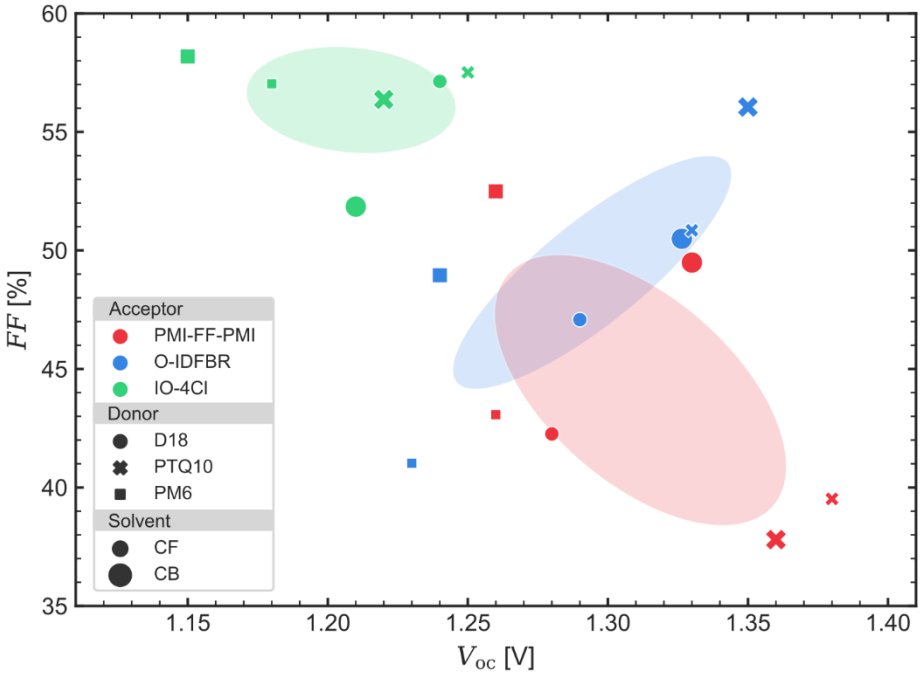

Figure S6: FF vs. V_{oc} for the 18 best devices. *The FF varies in a lower range compared to J_{sc} which is why it does not have such an important impact in the final PCE as the J_{sc}has. There is no clear correlation between FF and V_{oc} since the 1σ elipses show that for IO-4Cl the correlation is negligible and for PMI-FF-PMI and O-IDFBR the correlation is negative and positive respectively.*

Section S7: V_{oc} losses calculations

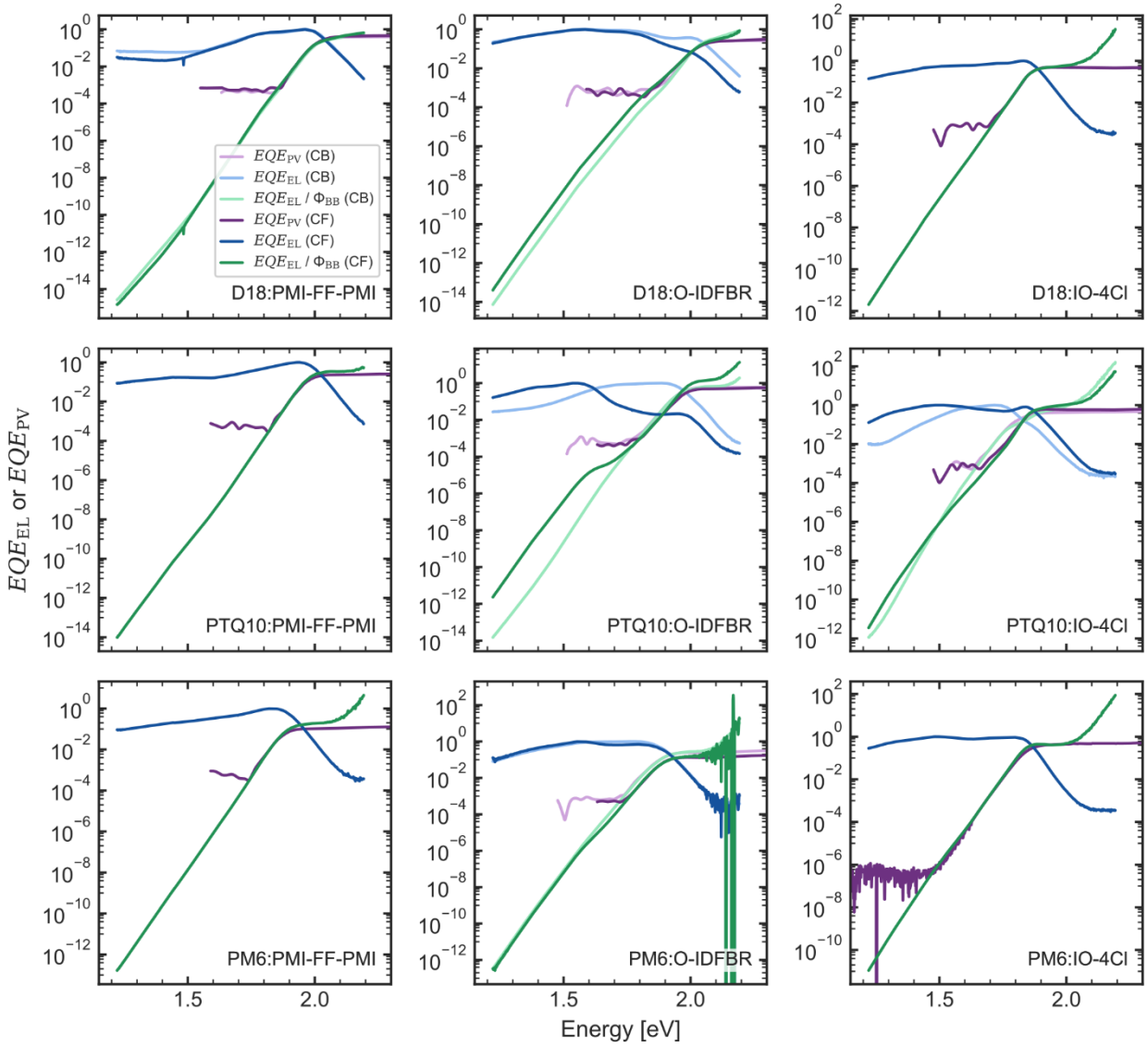

Figure S5: EL fits for extend the EQE_{PV} for V_{oc} losses calculations. *The EL spectrum divided by the BB spectrum (green) is fitted to the EQE_{PV} (purple) in low energy EQE_{PV} region where the EQE_{PV} edge shows a slope in a logarithmic scale. The plots also show the EL resulting from the fitted spectrum (blue). The light and dark colors stand for CF and CB respectively. The data from the blends D18:IO-4Cl, PTQ10:PMI-FF-PMI, PM6:PMI-FF-PMI and PM6:IO-4Cl prepared by CB is missing because they were not measured.*

In order to properly calculate V_{oc} voltage losses one needs the photovoltaic external quantum efficiency (EQE_{PV}) in a large spectral and dynamic range. The standard EQE_{PV} characterization (which was done in this work) comprising an arc-lamp light source and a monochromator is not enough for a proper characterization of V_{oc} losses. According to Rau,[4] EQE_{PV} of a solar cell is equivalent to the quotient between the electroluminescence quantum efficiency (EQE_{EL}) and the black body spectrum (ϕ_{BB}). EQE_{EL} is understood as the spectral distribution of the photons emitted by the cell when a current is applied to it. Its integral over the spectrum has to account for the total number of emitted photons per injected electron (expressed in %). This measure is difficult to perform due to the challenge of collecting all emitted photons because their emission is generally omnidirectional. Nevertheless, assuming that the spectral shape is homogeneous in all directions and taking advantage of the relation between EQE_{EL} and EQE_{PV}, we can

assess EQE_{EL} by measuring the EL spectrum (ϕ_{EL}) and the EQE_{PV}. This is done by assuming that $EQE_{\mathrm{EL}} = a \cdot \phi_{\mathrm{EL}}$, where a is a factor that is fitted to the relation between EQE_{PV} and EQE_{EL}:

$$EQE_{\mathrm{PV}} = \frac{EQE_{\mathrm{EL}}}{\phi_{\mathrm{BB}}} = \frac{\mathrm{a} \cdot \phi_{\mathrm{EL}}}{\phi_{\mathrm{BB}}}$$

Figure S5 shows the EQE_{EL} (in blue) as well as the EQE_{PV} and the $EQE_{\mathrm{EL}}/\phi_{\mathrm{BB}}$. The fitting of the factor a is done in the range where EQE_{PV} and ϕ_{EL} overlap which is around the energy band gap of the material. The final extended EQE_{PV} used for the V_{oc} analysis is taken as $EQE_{\mathrm{EL}}/\phi_{\mathrm{BB}}$ for energies below the fit range, the measured EQE_{PV} for energies above the fit range and the average between $EQE_{\mathrm{EL}}/\phi_{\mathrm{BB}}$ and EQE_{PV} inside the fit range.

Active layer materials			**$J-V$ curve**	**$V_{\mathrm{oc}}^{\mathrm{r}}$ calculations**		
Donor	Acceptor	Solvent	$J_{\mathrm{sc}}^{\mathrm{measured}}$ $[mA/cm^2]$	J_{sc} $[mA/cm^2]$	J_0 $[mA/cm^2]$	$V_{\mathrm{oc}}^{\mathrm{r}}$ $[V]$
D18	PMI-FF-PMI	CB	4.95	4.94	7.60×10^{-28}	1.66
D18	PMI-FF-PMI	CF	5.05	5.59	8.92×10^{-28}	1.65
D18	O-IDFBR	CB	3.85	3.34	1.25×10^{-27}	1.63
D18	O-IDFBR	CF	4.48	3.76	6.46×10^{-27}	1.59
D18	IO-4Cl	CF	8.32	7.65	3.95×10^{-25}	1.51
PTQ10	PMI-FF-PMI	CF	3.44	3.12	2.14×10^{-27}	1.62
PTQ10	O-IDFBR	CB	9.06	8.31	1.37×10^{-26}	1.59
PTQ10	O-IDFBR	CF	7.97	7.27	2.68×10^{-25}	1.51
PTQ10	IO-4Cl	CB	7.47	7.62	2.01×10^{-24}	1.46
PTQ10	IO-4Cl	CF	10.53	10.16	8.80×10^{-25}	1.49
PM6	PMI-FF-PMI	CF	2.16	1.94	3.63×10^{-26}	1.53
PM6	O-IDFBR	CB	5.00	4.43	1.35×10^{-25}	1.52
PM6	O-IDFBR	CF	5.93	2.38	7.37×10^{-26}	1.52
PM6	IO-4Cl	CF	9.83	7.05	1.32×10^{-24}	1.47

Table S5: Results from V_{oc} losses measurements and calculations.

Active layer materials			V_{oc} values				V_{oc} losses			
Donor	Acceptor	Solvent	V_{oc} $[V]$	V_{oc}^{r} $[V]$	V_{oc}^{SQ} $[V]$	E_{ba} [eV]	ΔV_{oc}^{nr} $[V]$	ΔV_{oc}^{r} $[V]$	ΔV_{oc}^{sc} $[V]$	ΔV_{oc}^{total} $[V]$
D18	PMI-FF-PMI	CB	1.28	1.66	1.71	2.01	0.38	0.02	0.03	0.73
D18	PMI-FF-PMI	CF	1.36	1.65	1.71	2.01	0.29	0.03	0.02	0.65
D18	O-IDFBR	CB	1.33	1.63	1.72	2.02	0.30	0.05	0.04	0.69
D18	O-IDFBR	CF	1.31	1.59	1.74	2.04	0.28	0.11	0.03	0.73
D18	IO-4Cl	CF	1.24	1.51	1.57	1.86	0.27	0.04	0.02	0.62
PTQ10	PMI-FF-PMI	CF	1.38	1.62	1.68	1.98	0.24	0.02	0.04	0.60
PTQ10	O-IDFBR	CB	1.35	1.59	1.65	1.95	0.24	0.04	0.02	0.60
PTQ10	O-IDFBR	CF	1.34	1.51	1.68	1.98	0.17	0.15	0.02	0.64
PTQ10	IO-4Cl	CB	1.19	1.46	1.54	1.83	0.27	0.05	0.02	0.64
PTQ10	IO-4Cl	CF	1.25	1.49	1.55	1.84	0.24	0.04	0.02	0.59
PM6	PMI-FF-PMI	CF	1.25	1.53	1.60	1.89	0.28	0.01	0.06	0.64
PM6	O-IDFBR	CB	1.19	1.52	1.60	1.89	0.33	0.04	0.04	0.70
PM6	O-IDFBR	CF	1.22	1.52	1.60	1.89	0.30	0.03	0.05	0.67
PM6	IO-4Cl	CF	1.16	1.47	1.55	1.84	0.31	0.05	0.02	0.68

Table S6: V_{oc} losses analysis results. *The V_{oc} values are the different V_{oc} calculated following the procedure on the main text of the article. The difference between them (V_{oc} increments) correspond to the different voltage losses associated to non-radiative(ΔV_{oc}^{nr}), radiative (ΔV_{oc}^{r}), and due to J_{sc} difference (ΔV_{oc}^{sc}). The total voltage loss is also shown (ΔV_{oc}^{total}).*

Section S9: LED references table

Kind	Active layer materials	Intensity [lux]	V_{oc} [V]	J_{sc} [uA/cm²]	FF [%]	PCE [%]	Ref.
Fullerene	PTB7-Th/$PC_{71}BM$	186	0.56	19	72	10.55	[5]
Fullerene	PTB7-Th/$PC_{71}BM$	890	0.62	92	74	11.63	[5]
Fullerene	PDTBTBz-$2F_{anti}$:$PC_{71}BM$	1000	0.82	112.4	70.4	23.1	[6]
Fullerene	P3HT:$PC_{71}BM$	1000	0.5	73.7	71.9	9.4	[6]
Fullerene	PBDB-T:$PC_{71}BM$	1000	0.67	90.2	71.3	15.3	[6]
Fullerene	PTB7:$PC_{71}BM$	1000	0.57	87.6	69.3	12.3	[6]
Fullerene	WF3:$PC_{71}BM$	500	0.57	58.3	64.2	12.83	[7]
Fullerene	WF3S:$PC_{71}BM$	500	0.61	60.4	65.7	14.32	[7]
Fullerene	WF3F:$PC_{71}BM$	500	0.69	63.6	67.4	17.34	[7]
Fullerene	P1:$PC_{71}BM$ (100 nm)	300	0.76	29.6	66.1	19.15	[8]
Fullerene	P1:$PC_{71}BM$ (200 nm)	300	0.76	28.2	67.2	18.43	[8]
Fullerene	P3HT:$PC_{61}BM$	500	0.43	62	59	8.9	[9]
Fullerene	P3HT:ICBA	500	0.73	50	63	13.05	[9]
Fullerene	PTB7:PNP	200	0.57	19	67	9.5	[10]
Fullerene	BDT-2T-ID:PNP	200	0.75	24.2	68	16	[10]
Fullerene	BDT-1T-ID:PNP	200	0.84	19.2	59	12.4	[10]
Fullerene	1DTP-1D:PNP	200	0.69	26.4	68	17.7	[11]
Fullerene	2DTP-1D:PNP	200	0.71	22.4	61	13.8	[11]
Fullerene	PCDTBT:$PC_{71}BM$	300	0.7	31.2	56.6	16	[12]
Fullerene	PTB7:$PC_{71}BM$	500	0.6	46	54.3	8.9	[12]
NFA	PPDT2FBT:ITIC-M	300	0.53	20.8	57	6.9	[13]
NFA	PPDT2FBT:ITIC-M	1000	0.62	68.5	54.6	7.5	[13]
NFA	PPDT2FBT:ITIC-F	300	0.29	34.8	31.3	3.5	[13]
NFA	PPDT2FBT:ITIC-F	1000	0.45	85.5	37.6	4.7	[13]
NFA	PPDT2FBT:tPDI_2N-EH	300	0.79	20.9	49.9	9	[13]
NFA	PPDT2FBT:tPDI_2N-EH	1000	0.84	65.4	50.2	8.9	[13]
NFA	CD1:ITIC	1000	0.77	107	67.5	15.4	[13]
NFA	CD1:PBN-10	1000	1.14	105	65.4	21.7	[13]
NFA	PBDB-TF:IO-4Cl (1cm^2)	200	1.03	18.2	71.5	22.2	[1]
NFA	PBDB-TF:IO-4Cl (1 cm^2)	1000	1.1	90.6	79.1	26.1	[1]
NFA	PBDB-TF:ITCC	1000	0.962	95.8	72.2	22	[14]
NFA	PBDB-TF:IT-4F	1000	0.712	113	78.0	20.8	[14]
NFA	PBDB-TF:IT-M	500	0.88	54.2	75.4	22.8	[15]
NFA	PM6:Y6-O	1650	0.84	245	76	30.9	[16]
NFA	P3TEA: FTTB-PDI4	1650	1.02	192	67	26.7	[16]
NFA	PM6:Y6	1000	0.72	146.6	77	36.5	[17]
NFA (This work)	PTQ10:O-IDFBR	560	1.21	57.7	58.5	22.6	This work
Multicomponent	PCDTBT:PDTSTPD:$PC_{71}BM$	300	0.72	31.4	62.1	18.1	[12]
Multicomponent	PTB7:$PC_{71}BM$:EP-PDI	500	0.65	57	68.5	15.4	[18]
Multicomponent	PTB7-Th:PBDB-T:ITIC-Th:$PC_{71}BM$	1000	0.68	102.3	57.5	14.3	[19]
Multicomponent	PTB7-Th:PBDB-T:$PC_{71}BM$:ITIC-Th	500	0.63	43.7	64.6	10.5	[20]
Multicomponent	PTB7-Th:PBDB-T:$PC_{71}BM$:ITIC-Th	1000	0.67	99.2	64.8	15.5	[20]
Multicomponent	PBDB-T:ITIC-Th:$PC_{71}BM$	1000	0.72	157	65.1	26.4	[21]
Multicomponent	PBDB-TF:Y6: Y–Th2	1000	0.701	320.1	74.48	22.7	[22]
Multicomponent	PM6:ITIC-Th:IT-4F	500	0.75	74.73	77.1	30.11	[23]

Table S7: References of the indoor literature comparison from Figure 6 c).

Section S10: Indoor LED spectrum CCT

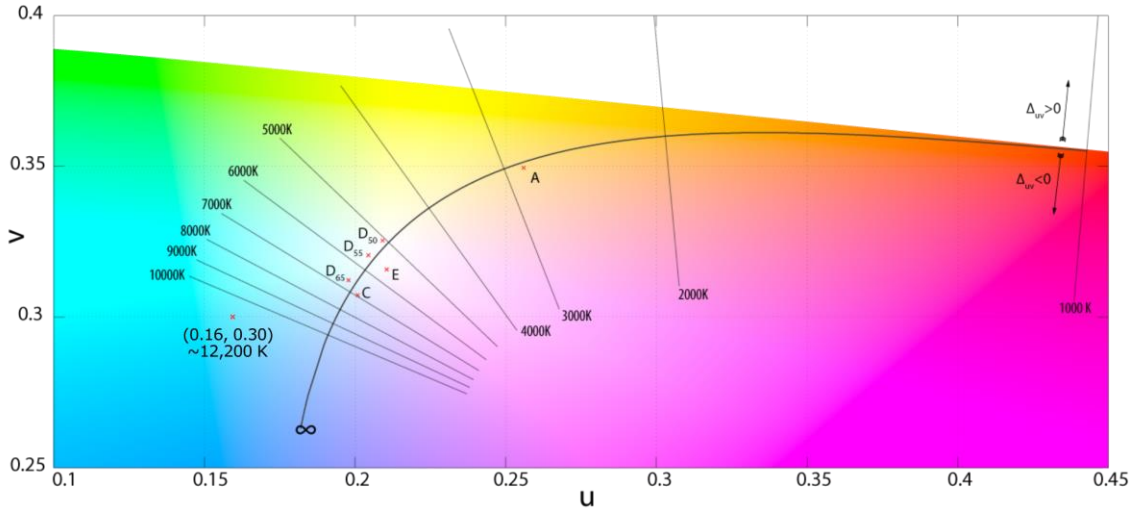

Figure S8: Color space representation for the indoor spectrum used. *CIE 1960 UCS color space where the Planckian locus is plotted (curved black line) from infinite to 10,000K temperature. Different temperature perpendicular lines are shown within* $\Delta_{uv} = \pm 0.05$ *that CIE considers the correlated color temperature (CCT) to be meaningful. Different reference spectra are positioned in the color space, as well as the LED spectrum used in this study, which has a* (u, v) *coordinates of (0.16, 0.30) corresponding to a CCT of 12,200 K. The* Δ_{uv} *is 0.031, therefore being inside the meaningful range of the CCT calculation as considered for CIE.*

Section S11: Indoor shunt resistance (R_{sh}) evaluation

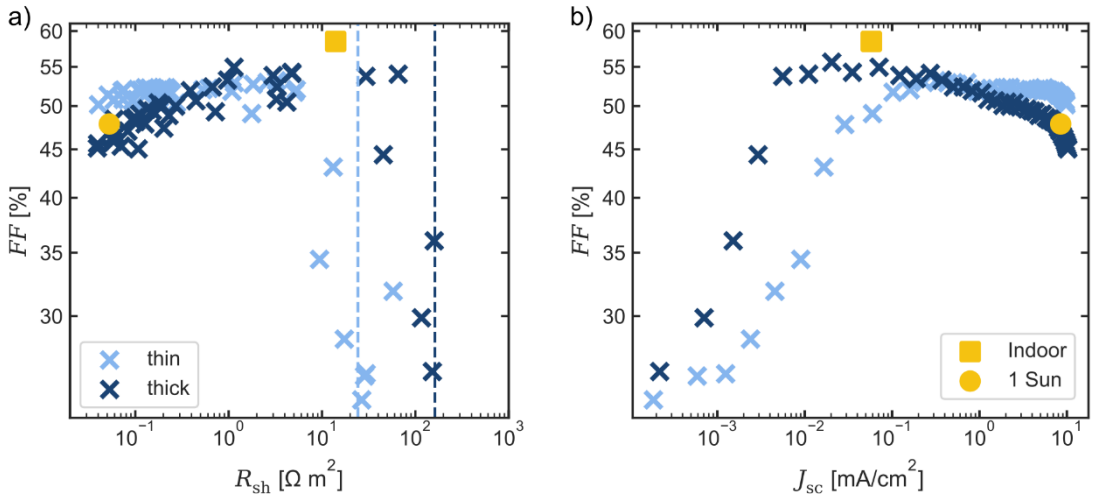

Figure S9: Evaluation PTQ10:O-IDFBR leakage with light-intensity dependent measurements. *(a) Fill factor (FF) plotted against shunt resistance (R_{sh}) for a thin (light blue crosses) and a thick (dark blue crosses) measured at different light intensities during a red sweep using the custom Spectrum On demand Light Source (SOLS) from ref. 25. Dashed vertical lines correspond to the R_{sh} of both cells measured in dark ($R_{sh,d}$). (b) FF vs. J_{sc} for the same data set. The yellow square in (a) and (b) corresponds to the data point of the solar cell measured under indoor conditions in the manuscript (figure 5). The yellow circle in (a) and (b) corresponds to the same cell measured under 1 Sun.*

Fill factor (FF) takes an important role in indoor light harvesting for OPV technology. In general, this is due to the inherent better charge dissociation for lower luminosities. At light intensities close to 1 sun, the main limiting factor is the series resistance (R_s). The effect of the latter decreases as light intensity, and so does photocurrent, decreases. This produces an increase in FF as light intensity decreases. On the opposite, at low intensities (close to indoor conditions) the performance of the solar cell is limited by leakage current, i.e. shunt resistance (R_{sh}).[24] This happens because, at low intensities, the photocurrent gets comparable to the leakage current. The limit when the J-V curve becomes a line without rectifying is when R_{sh} is approaching the sunt resistance at dark ($R_{sh,\,d}$).

We have measured J-V curves of two PTQ10:O-IDFBR at different light intensities in a wide dynamic range. The latter was done with a custom made equipment named spectrum on demand light source (SOLS). The data points are the result of a red sweep measurement. For more information you can check the corresponding publication of the SOLS.[25] It means that different light intensities were achieved by blocking the blue part of the solar spectrum maintaining the red fraction constant. This implies that the spectrum at each data point does not have the same shape. Nevertheless, assuming that the generated charges thermalize before they are extracted, the shape variance of the spectrum is not an issue. Therefore, as a first approximation J_{sc} is the parameter analogous to the light intensity when the latter is maintained with a constant spectral shape. Figure S9 (a) shows the FF vs. R_{sh} for the red sweep of two PTQ10:O-IDFBR cells with different thicknesses (blue data crosses). The vertical lines show the $R_{sh,\,d}$ for both devices. As expected, the thicker device (dark blue) has a higher $R_{sh,\,d}$ due to lower leakage current. The latter results in a FF higher than the thin device (light blue) at lower intensities. On the opposite, at high intensities, the thin cell exhibits a higher FF due to its lower series resistance produced by a thinner active layer. The yellow square and round data points corresponds to the solar cell characterized in indoor conditions in the manuscript for indoor illumination and 1 sun illumination, respectively. This cell at 1 sun has a FF in between the other two cells. Therefore, at indoor conditions we expect this cell to behave in between the blue data points, with a $R_{sh,\,d}$ in the middle. The corresponding square yellow data point is inside the expected trend exhibiting a high FF at R_{sh} just below the of $R_{sh,\,d}$ of the thinner device.

Similarly, Figure S9 (b) shows the FF vs. J_{sc} for the same red sweep measurements. The tendency is the expected since the thicker device (dark blue) exhibit a higher FF at low J_{sc} (i.e. low luminosity) while the thinner (light blue) shows higher FF at the J_{sc} region near 1-sun illumination. As happens in Figure S9 (a), the yellow datapoints, corresponding to the cell measured at indoor for indoor illumination (yellow square) and 1 sun illumination (yellow circle) are also in between the other two cells.

S.I. References

1 Y. Cui, Y. Wang, J. Bergqvist, H. Yao, Y. Xu, B. Gao, C. Yang, S. Zhang, O. Inganäs, F. Gao and J. Hou, *Nat Energy*, 2019, **4**, 768–775.

2 Y. Yang, C. Xue, H. Yin, Z. Chen and X. T. Hao, *Cell Rep Phys Sci*, 2022, **3**, 100861.

3 J. Hofinger, S. Weber, F. Mayr, A. Jodlbauer, M. Reinfelds, T. Rath, G. Trimmel and M. C. Scharber, *J Mater Chem A Mater*, 2022, **10**, 2888–2906.

4 U. Rau, *Phys Rev B Condens Matter Mater Phys*, 2007, **76**, 085303.

5 S. Mori, T. Gotanda, Y. Nakano, M. Saito, K. Todori and M. Hosoya, *Jpn J Appl Phys*, 2015, **54**, 071602.

6 Y. J. You, C. E. Song, Q. V. Hoang, Y. Kang, J. S. Goo, D. H. Ko, J. J. Lee, W. S. Shin and J. W. Shim, *Adv Funct Mater*, 2019, **29**, 1901171.

7 R. Singh, C. L. Chochos, V. G. Gregoriou, A. D. Nega, M. Kim, M. Kumar, S. C. Shin, S. H. Kim, J. W. Shim and J. J. Lee, *ACS Appl Mater Interfaces*, 2019, **11**, 36905–36916.

8 H. Yin, S. Chen, S. H. Cheung, H. W. Li, Y. Xie, S. W. Tsang, X. Zhu and S. K. So, *J Mater Chem C Mater*, 2018, **6**, 9111–9118.

9 S. S. Yang, Z. C. Hsieh, M. L. Keshtov, G. D. Sharma and F. C. Chen, *Solar RRL*, 2017, **1**, 1700174.

10 R. Arai, S. Furukawa, Y. Hidaka, H. Komiyama and T. Yasuda, *ACS Appl Mater Interfaces*, 2019, **11**, 9259–9264.

11 R. Arai, S. Furukawa, N. Sato and T. Yasuda, *J Mater Chem A Mater*, 2019, **7**, 20187–20192.

12 H. Yin, J. K. W. Ho, S. H. Cheung, R. J. Yan, K. L. Chiu, X. Hao and S. K. So, *J Mater Chem A Mater*, 2018, **6**, 8579–8585.

13 S. V. Dayneko, M. Pahlevani and G. C. Welch, *ACS Appl Mater Interfaces*, 2019, **11**, 46017–46025.

14 Y. Cui, H. Yao, T. Zhang, L. Hong, B. Gao, K. Xian, J. Qin, J. Hou, Y. Cui, H. Yao, T. Zhang, L. Hong, B. Gao, K. Xian, J. Qin and J. Hou, *Advanced Materials*, 2019, **31**, 1904512.

15 V. Shrotriya, G. Li, Y. Yao, T. Moriarty, K. Emery and Y. Yang, *Adv Funct Mater*, 2006, **16**, 2016–2023.

16 L.-K. Ma, Y. Chen, P. C. Y. Chow, G. Zhang, J. Huang, C. Ma, J. Zhang, H. Yin, A. M. Hong Cheung, K. S. Wong, S. K. So and H. Yan, *Joule*, 2020, **4**, 1486–1500.

17 C. Lee, J. Lee, H. H. Lee, M. Nam and D. Ko, *Adv Energy Mater*, , DOI:10.1002/aenm.202200275.

18 R. Singh, S. C. Shin, H. Lee, M. Kim, J. W. Shim, K. Cho and J. J. Lee, *Chemistry – A European Journal*, 2019, **25**, 6154–6161.

19 M. Nam, H. Yeon Noh, J. Cho, Y. Park, S.-C. Shin, J.-A. Kim, J. Kim, H. Hwi Lee, J. Won Shim, D.-H. Ko, M. Nam, H. Y. Noh, J. Cho, Y. Park, J. Kim, D. Ko, S. Shin, J. W. Shim, J. Kim and H. H. Lee, *Adv Funct Mater*, 2019, **29**, 1900154.

20 M. Nam, H. Y. Noh, J. H. Kang, J. Cho, B. K. Min, J. W. Shim and D. H. Ko, *Nano Energy*, 2019, **58**, 652–659.

21 M. Nam, J. Kang, J. Shin, J. Na, Y. Park, J. Cho, B. Kim, H. Hwi Lee, R. Chang, D.-H. Ko, M. Nam, J. Kang, J. Shin, J. Cho, B. Kim, D. Ko, J. Na, Y. Park, R. Chang and H. H. Lee, *Adv Energy Mater*, 2019, **9**, 1901856.

22 Y. Cho, T. Kumari, S. Jeong, S. M. Lee, M. Jeong, B. Lee, J. Oh, Y. Zhang, B. Huang, L. Chen and C. Yang, *Nano Energy*, 2020, **75**, 104896.

23 T. H. Kim, N. W. Park, M. A. Saeed, S. Y. Jeong, H. Y. Woo, J. Park and J. W. Shim, *Nano Energy*, 2023, **112**, 108429.

24 D. Lübke, P. Hartnagel, M. Hülsbeck and T. Kirchartz, *ACS Materials Au*, 2023, **3**, 215–230.

25 M. Casademont-Viñas, M. Gibert-Roca, M. Campoy-Quiles and A. R. Goñi, *Review of Scientific Instruments*, 2023, **94**, 103907.